Materials Advances

ROYAL SOCIETY OF CHEMISTRY

PAPER

View Article Online
View Journal | View Issue

Cite this: *Mater. Adv.*, 2022, 3, 5468

Synergy of backbone and end-group engineering for efficient non-fused-ring asymmetric electron acceptor-based organic solar cells†

Can Qian,‡ Jianing Zhu,‡ Dawei Sun,‡ Hao Xia, Jiali Guo, Jinhui Zhao, Mengbing Zhu, Hua Tan, * Xin Song* and Weiguo Zhu *

Silole-based building blocks have been used to construct simple non-fused-ring electron acceptors (EAs) due to their improved packing ability and high charge mobility. However, most of these EAs have an A–D′–D–D′–A framework with three symmetric central units and exhibit lower power conversion efficiency (PCE) in organic solar cells (OSCs). In order to further simplify the molecular framework and get an improved PCE, in this work, two silole-based non-fused-ring small-molecule electron acceptors (EAs) of **DTS26-IT-4F** and **DTS26-IT-4Cl** were designed and synthesized with an A–D–D′–A backbone, in which a dual electron-donating D–D′ assembly of dithienosilole (DTS) and asymmetric iso-octoxy indenothiophene (IT) is employed as a central building block. At the same time, the electronic properties, charge transport, and film morphology can be precisely tuned by modifying the end groups. Due to the synergistic effect of asymmetric D–D′ combination, both EAs exhibit a good planar molecular backbone and a large dipole, which result in an improved molecular aggregation. Meanwhile, **DTS26-IT-4Cl** with chlorinated end groups and larger dipole moments exhibited lower LUMO energy levels. An outstandingly boosted PCE of 11.00% with a high open-circuit voltage of 0.878 V was achieved with the **DTS26-IT-4Cl**-based binary OSCs using polymer PM6 as the donor material. This work indicates that the asymmetric D–D′ assembly along with regulation of end-group engineering is a promising central building block to obtain high-performance EAs by their synergy.

Received 3rd April 2022,
Accepted 14th May 2022

DOI: 10.1039/d2ma00382a

rsc.li/materials-advances

1. Introduction

As one of the most promising energy technologies in the 21st century, organic solar cells (OSCs) have received extensive attention for renewable energy owing to their advantages of light weight, flexibility, and large-area fabrication.[1–5] With the significant merits of non-fullerene small-molecule electron acceptors (EAs), OSCs have made a huge breakthrough in which the power conversion efficiency (PCE) has exceeded 20%.[6] Nowadays, most of the high-performance EAs have A–D–A and A_1–D_1AD_1–A_1 structures with a multi-fused-ring central unit,[7–9] such as ITIC[8] or Y6,[9] which exhibits intramolecular charge transfer and extended absorption through a push–pull electronic effect. Moreover, the intermolecular stacking, absorption, energy levels, chemical stability and device stability were efficiently manipulated by tailoring the molecular conformation.[10–15] However, the complex synthesis steps and high cost of these EAs restrict their commercial applications. Therefore, the development of simple non-fused-ring EAs is crucial for OSCs.

In order to obtain simple-structures and non-fused-ring Eas with high efficiency, two strategies have been recently developed. The first is a conformation-locked strategy. By the resulting non-covalent bonds, such as O–S, N–S, X–S (X = halogen) and hydrogen bonds, in this way, the molecular backbones can be tuned to have better planarity and rigidity, and furthermore their molecules can exhibit a more enhanced crystallization, and better solubility and processing than the fused-ring electron acceptors (FREAs) besides having simple synthesis steps.[16] For example, Huang *et al.* introduced S···O non-covalent interactions to obtain a simple molecule BTzo-4F with a PCE of 13.8%.[17] Chen *et al.* utilized O···H non-covalent interactions to construct a simple molecule PTIC with a PCE of 13.97%.[18] Bo *et al.* designed a simple molecule FOC6-FIC by introducing both S···O and S···F non-covalent interactions and it exhibited a PCE

School of Materials Science and Engineering, Jiangsu Collaboration Innovation Center of Photovoltaic Science and Engineering, Jiangsu Engineering Laboratory of Light-Electricity-Heat Energy-Converting Materials and Applications, National Experimental Demonstration Center for Materials Science and Engineering, Changzhou University, Changzhou 213164, P. R. China.
E-mail: zhuwg18@126.com, tanhua815@126.com, xin.song@cczu.edu.cn

† Electronic supplementary information (ESI) available. See DOI: https://doi.org/10.1039/d2ma00382a

‡ The first three authors contributed equally.

of 12.08%.[19] Another promising approach is asymmetric framework manipulation. The resulting asymmetric molecules, in this way, have an increased dipole moment and are beneficial for overcoming the Coulomb binding energy, which can increase intermolecular forces and improve the exciton dissociation.[20–26] For instance, Tang *et al.* developed a simple asymmetric acceptor based on dithieno[3, 2-*b*:2′,3′-*d*] pyrrole (DTP), named DBT-4F with an A–D_1–D–D_2–A framework, and obtained a PCE of 12.14%.[27] Yang *et al.* synthesized a novel asymmetric EA of AY6 by replacing benzodicyclopentadiene (BDC) with benzothiadiazole pyrrole (BTP) and achieved an advanced PCE of 15.6%.[28] Yan *et al.* introduced different end groups on both sides of BTP to synthesize another novel asymmetric EA (BTP-2ThCl), and acquired a PCE of 14.49%.[29] However, simple-structure and non-fused-ring EAs are rarely reported with both asymmetric and conformational-lock characters.

According to previous research reports, introduction of silole-based building blocks into polymer donors can improve molecular accumulation and charge mobility. Most of the introduced silole-based building blocks are dithienosilole, dibenzosilole and silaindace-nodithiophene (SiIDT).[30–33] Compared with the sp^3 hybrid C atom, the sp^3 hybrid Si atom can promote its electron-withdrawing ability to exhibit an increased intramolecular charge-transfer (ICT) effect, and furthermore the lowest unoccupied molecular orbital (LUMO) energy level, which is conducive to obtaining a higher open-circuit voltage (V_{OC}) in PSCs.[34] Meanwhile, by connecting different units in the silole-based building blocks, the stacking conformation and charge mobility of the silole-based molecules can be tuned, suggesting their great potential applications in the organic electronic field.[35,36]

In general, end-group engineering can modulate the absorption, mobility, and energy levels of materials by altering their electron-withdrawing capabilities and intermolecular interactions.[37] For example, Hou *et al.* reported an EA of BTP-4Cl by introducing Cl atoms to replace F atoms on both sides of BTP-4F and obtained an increased PCE of 16.5%.[38] Huang *et al.* introduced an extended π-conjugation end group and tuned the degree of polyfluorination in EAs to achieve an advanced PCE of 14.53%.[39] Hou *et al.* introduced thienyl-fused indanone as an end-group on both sides of ITIC to synthesize another EA (ITCC) and acquired a PCE of 11.4%.[40] Based on the above opinion, rational design of simple-structure, non-fused-ring and silole-containing EAs should be of great significance to obtain high-performance OSCs.

However, most of these non-fused-ring and silole-containing EAs have an A–D′–D–D′–A framework with three symmetric central units and exhibited a lower PCE in OSCs. In order to further simplify the molecular framework and get an improved PCE, in this work, a dual electron-donating D–D′ assembly of

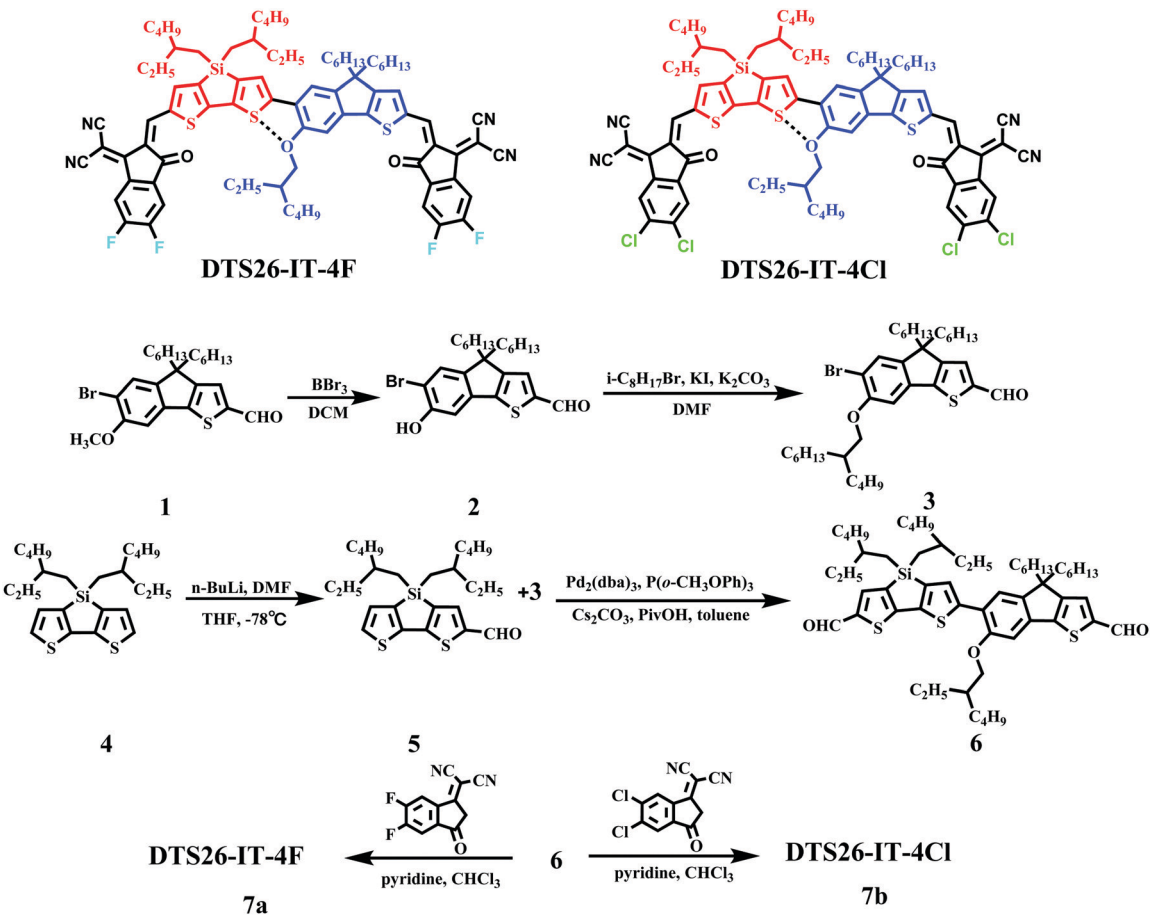

Scheme 1 Synthetic route for **DTS26-IT-4F** and **DTS26-IT-4Cl**.

symmetric dithienosilole (DTS) and asymmetric isooctoxy indenothiophene (IT) was primarily applied as a central building block to construct two simple-structures, non-fused-ring and silole-containing EAs with a simple A–D–D′–A framework. Scheme 1 shows their molecular structures and the synthetic route of both molecules, named **DTS26-IT-4F** and **DTS26-IT-4Cl**, respectively, with fluorine- and chlorine-substituted end groups of 2-(3-oxo-2,3-dihydro-1*H*-inden-1-ylidene) malono-nitrile (IC). The design principle of the strong electron donor group DTS in our target molecule would enhance the push–pull (D–A) action with the aim of a broad absorption range. In addition, the introduction of the asymmetric unit DTI with alkoxy chains would build a non-covalent bonding lock with the DTS block, resulting in better planarity and increased intermolecular forces, thereby improving the crystallinity and charge mobility of the acceptor. At the same time, F atoms and Cl were introduced on the IC group to enhance the ICT effect. The synergistic effect of the asymmetric D–D′ assembly and end groups of the substituted IC on the photophysical, electrochemical and photovoltaic properties, as well as the crystallinity, morphology and carrier mobility, were systematically studied. All two unfused acceptors exhibit strong absorption from the visible to near infrared region, corresponding to an optical band gap (E_g^{opt}) below 1.45 eV. Improved crystallinity, absorption and charge mobility were observed by the combined introduction of asymmetric isooctoxy IT and symmetric DTS and different end groups. Furthermore, an outstandingly advanced PCE of over 11.00% with a high V_{OC} of 0.878 V was obtained in the binary OSCs using polymer PM6 as the donor and DTS26-IT-DCl as the acceptor. Our work demonstrated that high-efficiency and simple-structure, non-fused-ring acceptors can be obtained with an asymmetric A–D–D′–A backbone by the synergistic effect of dithienosilole and isooctoxy IT.

2. Results and discussion

2.1 Synthesis, characterization, and thermal properties

The synthetic route of **DTS26-IT-4F** and **DTS26-IT-4Cl** is described in Scheme 1 and their synthetic procedures are described in the ESI.† **DTS26-IT-4F** and **DTS26-IT-4Cl** were obtained by five reactions. Their molecular structures were characterized by ^{1}H-NMR and mass spectrometry (S12–S19), as shown in the ESI.† Differential scanning calorimetry (DSC) measurements were carried out in a nitrogen atmosphere between 50 and 300 °C, at a heating or cooling rate of 10 °C min^{-1} and these two small molecules did not show a distinct signal in the DSC curves. The corresponding curves are shown as insets in Fig. S1 (ESI†). The thermal properties of both EAs were tested by thermogravimetric analysis (TGA) and their TGA curves are shown in Fig. S2 (ESI†). It is found that both EAs exhibited a high thermal decomposition temperature (T_d) at 5% weight loss. The resulting T_d values are 358 °C for **DTS26-IT-4F** and 365 °C for **DTS26-IT-4Cl**. Therefore, this type of simple-structure, non-fused-ring and silole-containing EA has excellent thermal stability.

2.2 Optical and electrochemical properties

The UV-Vis absorption spectra of **DTS26-IT-4F** and **DTS26-IT-4Cl** in thin films and diluted chloroform solutions (10^{-5} M) are shown in Fig. 1(a) and Fig. S3 (ESI†). The relevant absorption data are summarized in Table 1. In chloroform solutions, both

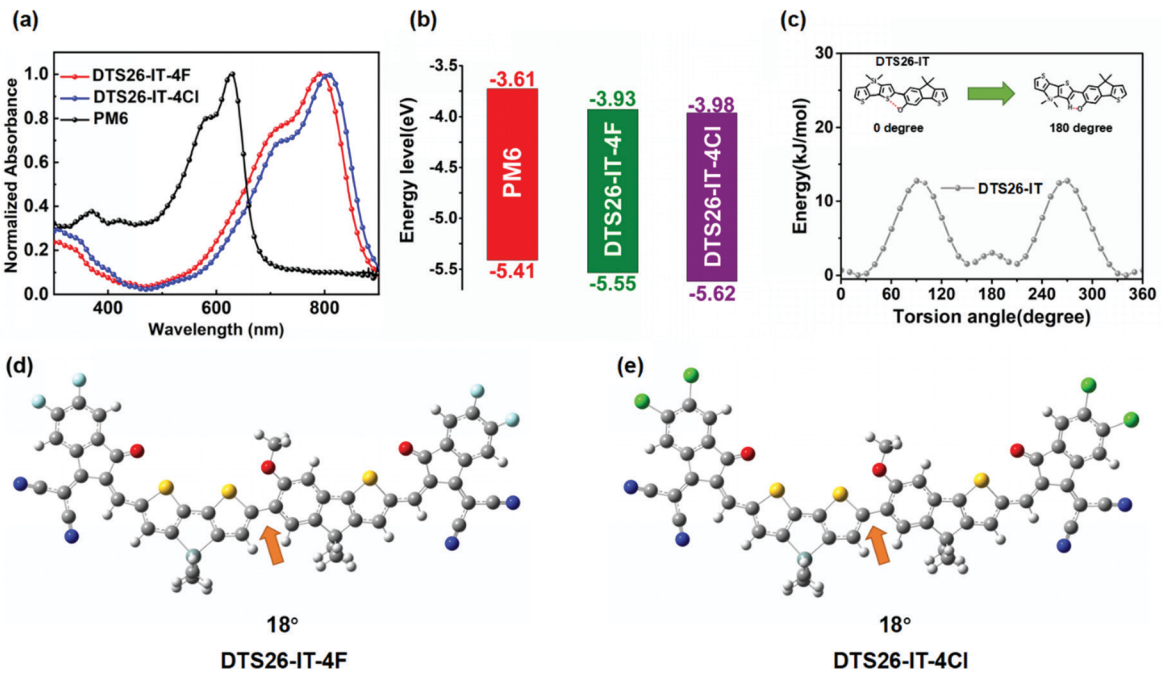

Fig. 1 (a) Normalized UV-Vis-NIR absorption spectra, (b) energy level diagrams of PM6, **DTS26-IT-4F** and **DTS26-IT-4Cl**, and (c) potential energy surface scan of the rotamer DTS26-IT, (d) molecular geometry of **DTS26-IT-4F** and (e) molecular geometry of **DTS26-IT-4Cl** calculated by DFT.

EAs exhibit a similar and strong absorption band in the wavelength range of 500–800 nm, which is attributed to their intra-molecular charge transfer (ICT). The absorption peak at 731 nm with the maximum molar extinction coefficient of 1.84×10^5 M^{-1} cm^{-1} is observed for the **DTS26-IT-4Cl** solution, which is red-shifted by 16 nm in comparison with the **DTS26-IT-4F** solution. From their solutions to films, both EAs exhibit broader and significantly red-shifted absorption spectra with a ~16 nm red shift. This implies that both EAs display more intense intermolecular interactions. The absorption maximum at 894 nm is found in the **DTS26-IT-4Cl** neat film. Obviously, Cl-substituted EA of **DTS26-IT-4Cl** exhibits a little red-shifted absorption profile in comparison with the F-substituted EA of **DTS26-IT-4F** in their solutions and neat films, which should be related to a more ordered stacking structure resulting from Cl substitution. Based on their absorption onsets in the films, the optical band gap (E_g^{opt}) values are calculated to be 1.41 eV for **DTS26-IT-4F** and 1.39 eV for **DTS26-IT-4Cl**. There is a more complementary absorption profile between polymer PM6 and **DTS26-IT-4Cl** instead of **DTS26-IT-4F**, which is beneficial for capturing more photoelectrons and boosting J_{SC} for their OSCs.

Fig. S4 (ESI†) shows the oxidation and reduction curves of both EAs *versus* Fc/Fc^+ measured by the cyclic voltammetry method (ESI†) and their electro-chemical data are summarized in Table 1. Reversible oxidation and reduction behaviors are observed for both EAs. The observed onset oxidation and reduction potentials (E_{ox}^{onset} and E_{red}^{onset}) are 0.73 V/−0.87 V for **DTS26-IT-4F** and 0.76 V/−0.84 V for **DTS26-IT-4Cl**. Based on the empirical equation, the highest occupied molecular orbital (HOMO) and the lowest unoccupied molecular orbital (LUMO) energy levels (E_{HOMO} and E_{LUMO}) are calculated to be −5.53 eV/−3.93 eV and −5.56 eV/−3.96 eV, respectively. It is clear that **DTS26-IT-4Cl** exhibits lower HOMO and LUMO energy levels than **DTS26-IT-4F**, which should be attributed to the partially larger dipole moment of chlorine-substituted molecules.[41] In comparison with EA using dual symmetric dithienosilole (DTS) units as a central unit, this type of EA with dual asymmetric D–D′ assembly exhibits a decreased HOMO energy level.[27]

2.3 Density functional theory calculations and crystallinity

In order to further understand the molecular conformations, the energy levels of the frontier molecular orbitals (FMOs) and the dipole moments of both EAs, we performed density functional theory (DFT) calculations for **DTS26-IT-4F** and **DTS26-IT-4Cl** at the B3LYP/6-31G(d,p) level. Fig. 1(c) shows the potential energy surface scan curve of the rotamer DTS26-IT. The lowest potential energy is at a torsion angle of ~20° between DTS and IT for both EAs. In the optimal conformations of DTS-IT-4F and DTS-IT-4Cl shown in Fig. 1(d) and (e), the calculated dihedral angle between the IT and DTS units is just 18° for DTS-IT-4F and DTS-IT-4Cl. This implies that both EAs exhibit quasi planarity. The small dihedral angle between the IT and DTS units should be related to the formed intramolecular O–S non-covalent bond. The calculated distance between the S atom in the DTS unit and the O atom at the alkoxy in IT is 2.77 Å, which is significantly shorter than the sum of the van der Waals radii of S and O (3.25 Å),[42] indicating the existence of a non-covalent conformational lock.[19]

Fig. S5 (ESI†) shows the electron cloud distributions of the frontier molecular orbitals and their energy levels for **DTS26-IT-4F** and **DTS26-IT-4Cl**. It is found that the electron clouds of the LUMO are distributed throughout the conjugated backbone. The ones of the HOMO are mainly located on the electron-donating D–D′ units, which facilitates electron transport. The calculated LUMO/HOMO energy levels are −3.47/−5.51 eV for DTS-IT-4F and −3.55/−5.56 eV for DTS-IT-4Cl, respectively, which is consistent with the CV results.

Fig. S6 (ESI†) shows the natural dipole moments of DTS26, IT, 2DTS26, DTS26-IT, 2IT, DTS26-IT-DF and DTS26-IT-DCl and their vector addition (μ_m) calculated by DFT. It is found that the dipole moments of DTS26 and IDT are 1.82 D and 0.59 D, respectively. When DTS26 and IT are coupled together, the dipole moments of 2DTS26 and 2IT are decreased to 0.09 D and 0.26 D, respectively. In contrast, the dipole moment of DTS26-IT is increased to 1.68 D, indicating that the asymmetric D–D′ structure exhibits a greater dipole moment than the symmetric D–D and D′–D′ structures. Therefore, both asymmetric EAs further exhibit a greater dipole moment. which is 2.57 D for **DTS26-IT-4F** and 2.87 D for **DTS26-IT-4Cl**, respectively. This indicates that the chlorine-substituted **DTS26-IT-4Cl** has a stronger ICT effect than fluorine-substituted **DTS26-IT-4F**,[40] which is consistent with the tested absorption spectra.

To better understand the crystallinity and stacking behaviors of both EAs, we performed their powder X-ray diffraction (PXRD) analysis. Fig. S7 (ESI†) shows the XRD patterns of the **DTS26-IT-4F** and **DTS26-IT-4Cl** (ESI†). The (100) diffraction peaks at 2θ = 5.35° and 5.75° are observed in **DTS26-IT-4F** and **DTS26-IT-4Cl** solid powders. The calculated *d*-spacing values are 16.51 Å for **DTS26-IT-4F** and 15.36 Å for **DTS26-IT-4Cl**, which is attributed to the lamellar stacking. In the wide-angle region, (010) diffraction peaks of 25.38° and 25.91° are observed for **DTS26-IT-4F** and **DTS26-IT-4Cl**, respectively. The calculated *d*-spacing values are 3.51 Å for **DTS26-IT-4F** and 3.44 Å for **DTS26-IT-4Cl** according to the Bragg equation. This indicates that **DTS26-IT-4Cl** exhibits a more ordered structure and tighter intermolecular π–π stacking, which is available to facilitate charge transport and increase the FF for its OSCs.

Table 1 Optical and electrochemical data of **DTS26-IT-4F** and **DTS26-IT-4Cl**

Acceptor	λ_{max}^{sol} (nm)	λ_{max}^{film} (nm)	λ_{oneset}^{film} (nm)	$E_g^{opt\,a}$ (eV)	$E_{LUMO}{}^b$ (eV)	$E_{HOMO}{}^b$ (eV)	ε (10^5 M^{-1} cm^{-1})
DTS26-IT-4F	716	791	879	1.41	−5.53	−3.93	1.42
DTS26-IT-4Cl	731	806	894	1.39	−5.56	−3.96	1.84

[a] The optical band gap calculated from the onset of pure film absorption. [b] $E_{HOMO} = -e(\varphi_{ox} + 4.80)$ (eV), $E_{LUMO} = -e(\varphi_{red} + 4.80)$ (eV).

2.4 Photovoltaic properties

To investigate the photovoltaic performance of both EAs when used as acceptors, their binary OSCs using polymer PM6 as a donor and one of the EAs as the acceptor were made with a conventional device structure of ITO/PEDOT:PSS/PM6:acceptor/PDIN/Ag. The processing conditions of the devices, such as PM6 : acceptor ratio, spin speed and additive dosage were optimized. The optimal PM6 : acceptor ratio of 1 : 1 and chloronaphthalene (CN) dosage of 0.5% was obtained. The photovoltaic parameters for these devices are summarized in Tables S1 and S2 (ESI†), under different processing conditions. Fig. 2(a) shows current density–voltage (J–V) curves of the optimized devices, respectively, based on the PM6:**DTS26-IT-4F** and PM6:**DTS26-IT-4Cl** blends at AM1.5, 100 mW cm^{-2} illumination. The optimal photovoltaic parameters are listed in Table 2 for the optimal devices. It is found that the optimized device with a PM6:**DTS26-IT-4Cl** blend exhibits better photovoltaic properties than the device with a PM6:**DTS26-IT-4F** blend. The PCE of 11.00% with a high V_{OC} of 0.878 V was obtained in the optimal PM6:**DTS26-IT-4Cl**-based device.

Fig. 2(b) depicts external quantum efficiency (EQE) curves of the optimized OSCs using both EAs as acceptors at different optical wavelengths. A wide-range photo-response from 300 to 900 nm is observed for the optimized OSCs, which is consistent with the light absorption of their corresponding blend films in Fig. S8 (ESI†). The integrated J_{SC} values are calculated to be 17.38 mA cm^{-2} for the optimal PM6:**DTS26-IT-4F** device and 18.25 mA cm^{-2} for the optimal PM6:**DTS26-IT-4Cl** device, which are consistent with the values obtained from the J–V curves within 5% mismatch. Indeed, in comparison with the optimal PM6:**DTS26-IT-4F** device, the optimal PM6:**DTS26-IT-4Cl** device exhibits a little broader and higher photo-response range, thus leading to a higher current density. This result indicates that the optimal PM6:**DTS26-IT-4Cl** device has a more efficient photo-response efficiency.

To better understand the performance enhancement after the terminal group modification, the charge extraction and exciton dissociation capabilities were investigated by measuring the relationship between photocurrent density (J_{ph}) *versus* effective voltage (V_{eff}). Fig. 2(c) shows the J_{ph}–V_{eff} curves of the optimal PM6:DT26-IT-4F- and PM6:DT26-IT-4Cl-based devices, and it is clear that the J_{ph} values of both optimal devices eventually reach the saturation current density (J_{sat}) when the V_{eff} applied is over 1.5 V. This indicates that all light-generated excitons here can dissociate into free carriers and be collected by the electrodes.[43,44] Moreover, we shed light on the current density under short-circuit conditions; according to the equation $P_{diss} = J_{ph}/J_{sat}$, we can calculate the exciton dissociation (P_{diss}) probabilities, where 92.03% and 92.53% are yielded for the optimal PM6:**DTS26-IT-4F**- and PM6:**DTS26-IT-4Cl**-based devices, respectively.[45] Higher P_{diss} value implies that the optimal PM6:**DTS26-IT-4Cl**-based device has a higher exciton dissociation and charge extraction efficiency, which is consistent with the EQE curve.

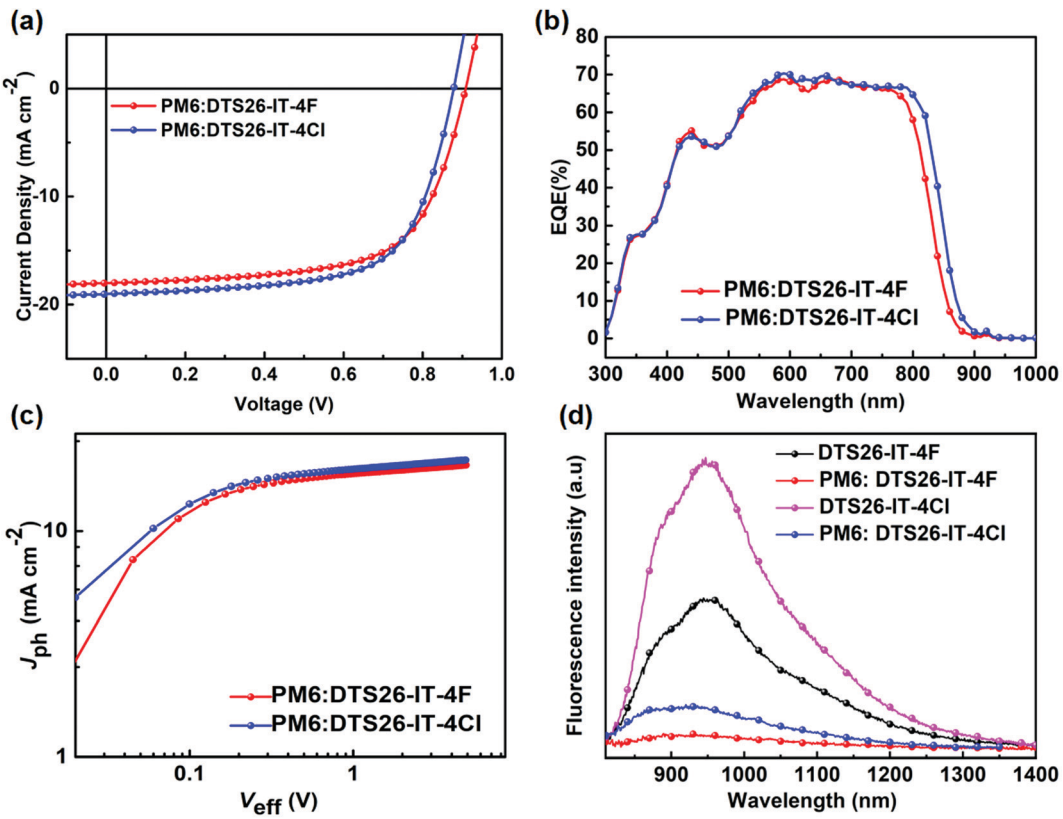

Fig. 2 (a) J–V curves, (b) EQE curves, and (c) J_{ph}–V_{eff} curves of the optimal PM6:**DT26-IT-4F** and PM6:**DT26-IT-4Cl** based OSCs. (d) PL spectra of the optimal PM6:**DTS26-IT-4F** and PM6:**DTS26-IT-4Cl** blend films, and **DTS26-IT-4F** and **DTS26-IT-4Cl** neat films excited at 780 nm.

Table 2 Optical parameters for **DTS26-IT-4F**- and **DTS26-IT-4Cl**-based optimal devices

Active layer	CN (%)	V_{OC} (V)	J_{SC} (mA cm^{-2})	J_{SC}^{a} (mA cm^{-2})	FF (%)	PCE^{b} (%)	μ_h/μ_e (10^{-5} cm^2 V^{-1} s^{-1})
DTS26-IT-4F	0.5	0.908	17.99	17.38	64.90	10.61 (10.55 ± 0.07)	7.80/6.80
DTS26-IT-4Cl	0.5	0.878	19.00	18.25	65.95	11.00 (10.71 ± 0.13)	9.91/8.60

[a] The integrated J_{SC} from EQE curves. [b] Average values and standard deviation within brackets.

In order to understand more clearly the reason why the PM6:**DTS26-IT-4Cl** OSCs displayed higher PCE value, we measured photoluminescence (PL) spectra of the optimal PM6:**DTS26-IT-4F** and PM6:**DTS26-IT-4Cl** blend films, as well as the DTS26-IT-4F and **DTS26-IT-4Cl** neat films under excitation of 780 nm light, as recorded in Fig. 2(d). It is found that the **DTS26-IT-4F** and **DTS26-IT-4Cl** neat films exhibit broad and strong PL emission in the range of 800–1400 nm. In contrast, in the optimal PM6:**DTS26-IT-4F** blend film, the PL is effectively quenched with a high PL quenching efficiency of 83.0%. Interestingly, in the optimal PM6:**DTS26-IT-4Cl** blend film, the PL quenching efficiency is increased to 90.3%. Therefore, the optimal PM6:**DTS26-IT-4Cl** blend film presents more effective photo-induced charge transfer behavior than the optimal PM6:**DTS26-IT-4F** blend film.[46,47]

2.5 Charge-transport properties

The hole-only devices of ITO/PEDOT:PSS/PM6:acceptor/MoO_3/Ag and electron-only devices of ITO/ZnO/PM6:acceptor/PFN/Al were made for determining the charge-transport properties. Fig. S9 (ESI†) shows the current density *vs* applied voltage semi-log characteristics of these hole-only and electron-only devices, respectively, using **DTS26-IT-4Cl** and **DTS26-IT-4F** as acceptors. Table 2 lists the calculated hole mobilities (μ_h) and electron mobilities (μ_e) of the optimal photoactive layers of PM6:acceptor by using the space charge limited current (SCLC) method. For the PM6:**DTS26-IT-4F** blend, the calculated μ_h and μ_e values are 7.80×10^{-5} cm^2 V^{-1} s^{-1} and 6.80×10^{-5} cm^2 V^{-1} s^{-1}, respectively, with a μ_h/μ_e ratio of 1.15. In contrast, for the PM6:**DTS26-IT-4Cl** blend, the calculated μ_h and μ_e values are 9.91×10^{-5} cm^2 V^{-1} s^{-1} and 8.60×10^{-5} cm^2 V^{-1} s^{-1}, respectively, with a μ_h/μ_e ratio of 1.15. Obviously, the optimal PM6:**DTS26-IT-4Cl** blend exhibits higher μ_h and μ_e values than those of the optimal PM6:**DTS26-IT-4F** blend, which is responsible for the suppressed charge recombination and enhanced charge extraction, and further higher FF and J_{SC} for the PM6:**DTS26-IT-4Cl** devices.

2.6 Morphology and miscibility

Fig. 3 and Fig. S10 (ESI†) show the surface phase separation images of the optimal blend films of PM6:**DTS26-IT-4F** and PM6:**DTS26-IT-4Cl** recorded by atomic force microscopy (AFM) and transmission electron microscopy (TEM) measurements. The root-mean-square (RMS) roughnesses of 2.17 and 2.01 nm are exhibited in height images for the PM6:**DTS26-IT-4F** and PM6:**DTS26-IT-4Cl** blend films, respectively. Moreover, the fibrous texture is also observed for both optimal blend films in the phase images, which is mainly caused by the polymer.[48] The observed small RMS roughness indicates that both blend films have become smooth with good morphology and miscibility.

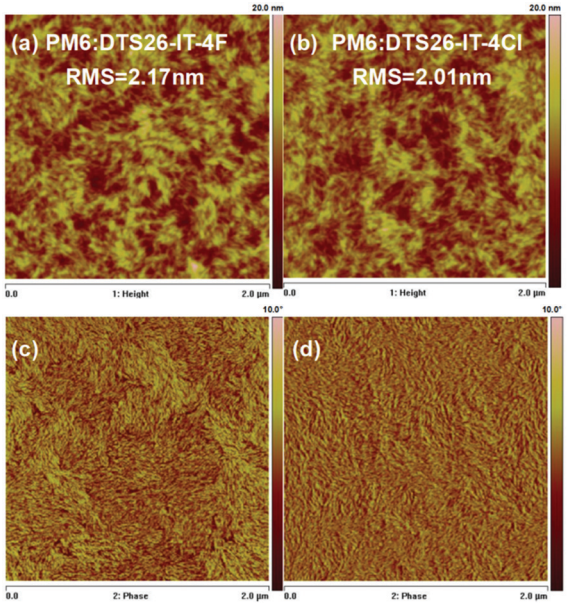

Fig. 3 AFM height and phase images for the optimal PM6:**DTS26-IT-4F** blend film (a and c) and PM6:**DTS26-IT-4Cl** blend film (c and d).

In addition, the TEM results are consistent with the AFM measurements. The PM6:**DTS26-IT-4Cl** blend film displays apparently more appropriate phase separation. The resulting fibrous texture implies that both blend films have formed continuous and interpenetrating networks, which is conducive to charge transport. Herein, the formed optimal morphology is beneficial to charge separation and transport, and further to obtaining higher J_{SC} and FF.

Generally, the morphology of the active layer is related to the miscibility of the acceptor and donor. The good morphology is due to the similar surface energies of the polymer donor and acceptor. Therefore, the molecule interaction can be calculated by contact angle measurements using deionized water as a polar liquid and diiodomethane as a non-polar liquid.[49] Fig. S11 (ESI†) shows the relevant profiles of the contact angles. The contact angles and surface energy data are presented in Table S3 (ESI†). Based on the equation $\delta = K\sqrt{\gamma}$, where γ is the surface energy of the materials and K is the constant of proportionality ($K = 116 \times 10^3$ m$^{-1/2}$), we calculated the solubility parameters (δ) for each component to investigate the miscibility of **DTS26-IT-4F** and **DTS26-IT-4Cl** in PM6.[50] Table 3 lists the surface energies, solubility parameters and absolute differences of PM6, the EAs and their blend films. It is suggested that, if the difference between the δ of two components (absolute value $\Delta\delta$) is smaller, the two materials should

Table 3 Surface energy (γ), solubility parameter (δ), and absolute difference of $\delta(\Delta\delta)$

Film	γ (mN m^{-1})	δ (Mpa$^{1/2}$)	$\Delta\delta$ (Mpa$^{1/2}$)
PM6	35.99	22.01	
DTS26-IT-4F	43.5	24.19	
DTS26-IT-4Cl	42.91	24.02	
PM6:**DTS26-IT-4F**			2.18
PM6:**DTS26-IT-4Cl**			2.01

$\Delta\delta = |\delta_{donor} - \delta_{acceptor}|$

be more mixed and easily lead to smaller phase separation.[50–54] Thus, the lower $\Delta\delta$ values of the blend film of PM6:**DTS-IT-4Cl** in comparison with that of PM6:**DTS-IT-4F** indicates that **DTS-IT-4Cl** and PM6 have better miscibility and exhibit a smaller phase separation with ideal blend morphology.

3. Conclusions

Two simple and high-efficiency non-fused-ring EAs of PM6:**DTS26-IT-4F** and PM6:**DTS26-IT-4Cl** were obtained with a D–D′ assembly of dithienosilole and isooctoxy indenothiophene. It is found that the D–D′ assembly strategy can facilely make both EAs form intramolecular conformation locks and asymmetric backbones. As a result, both EAs exhibit a relatively rigid planar structure and an improved inter-molecular effect by the synergy of intramolecular non-covalent interactions and asymmetric effects. The larger dipole moment of the chlorinated end group resulted in a lower LUMO level for **DTS26-IT-4Cl**. An advanced PCE of 11% with a high V_{OC} of 0.88 V was obtained with the PM6:**DTS26-IT-4Cl**-based binary OSCs. This work demonstrates that the synergy of non-covalent conformational locks and asymmetric structures along with the regulation of end-group engineering is a simple and effective strategy to obtain simple and high-efficiency non-fused-ring asymmetric EAs. Compared with high-efficiency non-fused small molecule acceptors, the two small molecules studied in this paper have lower J_{SC} and FF for several reasons: (1) low electron mobility induced by moderate crystallinity of the DTS building block. From several studies,[35,55,56] the poor molecular packing of DTS-based small molecules induces a relatively lower FF, which is always related to the charge transport capability. For the PM6:**DTS26-IT-4F** and PM6:**DTS26-IT-4F** blends, the calculated μ_e values are 6.80×10^{-5} cm^2 V^{-1} s^{-1} and 8.60×10^{-5} cm^2 V^{-1} s^{-1}, respectively, which is lower than that of the high efficiency system ($\sim 10^{-4}$ cm^2 V^{-1} s^{-1}). (2) As shown by TEM (Fig. S10, ESI†), the nano-fibrillar structures in the blends do not achieve ideal phase separation between charge transport and recombination.

Conflicts of interest

There are no conflicts of interest to declare.

Acknowledgements

Thanks is given for the financial support from the National Natural Science Foundation of China (51673031, 52073035), the Research Innovation Program for Postgraduate of Jiangsu Province (KYCX20_2513, KYCX21_2776, and SJCX21_1247), the Top-notch Academic Programs Project of Jiangsu Higher Education Institutions (TAPP), the Priority Academic Program Development of Jiangsu Higher Education Institutions (PAPD), and Jiangsu Provincial Talents Project of High-Level Innovation and Entrepreneurship.

References

1 Q. Guo, R. Ma, J. Hu, Z. Wang, H. Sun, X. Dong, Z. Luo, T. Liu, X. Guo, X. Guo, H. Yan, F. Liu and M. Zhang, *Adv. Funct. Mater.*, 2020, **30**, 2000383.
2 S. Pang, X. Zhou, S. Zhang, H. Tang, S. Dhakal, X. Gu, C. Duan, F. Huang and Y. Cao, *ACS Appl. Mater. Interfaces*, 2020, **12**, 16531–16540.
3 H. Wang, J. Cao, J. Yu, Z. Zhang, R. Geng, L. Yang and W. Tang, *J. Mater. Chem. A*, 2019, **7**, 4313–4333.
4 P. Cheng and Y. Yang, *Acc. Chem. Res.*, 2020, **53**, 1218–1228.
5 P. Cheng, J. Wang, X. Zhan and Y. Yang, *Adv. Energy Mater.*, 2020, **10**, 2000746.
6 Z. Zheng, J. Wang, P. Bi, J. Ren, Y. Wang, Y. Yang, X. Liu, S. Zhang and J. Hou, *Joule*, 2021, **6**, 171.
7 C. Yan, S. Barlow, Z. Wang, H. Yan, A. K.-Y. Jen, S. R. Marder and X. Zhan, *Nat. Rev. Mater.*, 2018, **3**, 18003.
8 Y. Lin, J. Wang, Z. G. Zhang, H. Bai, Y. Li, D. Zhu and X. Zhan, *Adv. Mater.*, 2015, **27**, 1170–1174.
9 J. Yuan, Y. Zhang, L. Zhou, G. Zhang, H.-L. Yip, T.-K. Lau, X. Lu, C. Zhu, H. Peng, P. A. Johnson, M. Leclerc, Y. Cao, J. Ulanski, Y. Li and Y. Zou, *Joule*, 2019, **3**, 1140–1151.
10 S. Dai, T. Li, W. Wang, Y. Xiao, T. K. Lau, Z. Li, K. Liu, X. Lu and X. Zhan, *Adv. Mater.*, 2018, **30**, e1706571.
11 Y. Cai, L. Meng, H. Gao, Z. Guo, N. Zheng, Z. Xie, H. Zhang, C. Li, X. Wan and Y. Chen, *J. Mater. Chem. A*, 2020, **8**, 5194–5199.
12 Y. Ma, D. Cai, S. Wan, P. Wang, J. Wang and Q. Zheng, *Angew. Chem., Int. Ed.*, 2020, **59**, 21627–21633.
13 X. Zhang, Y. Ding, H. Feng, H. Gao, X. Ke, H. Zhang, C. Li, X. Wan and Y. Chen, *Sci. China: Chem.*, 2020, **63**, 1799–1806.
14 T. J. Aldrich, S. M. Swick, F. S. Melkonyan and T. J. Marks, *Chem. Mater.*, 2017, **29**, 10294–10298.
15 T. J. Aldrich, M. Matta, W. Zhu, S. M. Swick, C. L. Stern, G. C. Schatz, A. Facchetti, F. S. Melkonyan and T. J. Marks, *J. Am. Chem. Soc.*, 2019, **141**, 3274–3287.
16 T. Liu, Q. Zhao, H. Wang, J. Qu, P. Chao, N. Zheng, H. Lai, D. Mo and F. He, *Mater. Chem. Front.*, 2019, **3**, 1859–1865.
17 X. Liu, Y. Wei, X. Zhang, L. Qin, Z. Wei and H. Huang, *Sci. China: Chem.*, 2020, **64**, 228–231.
18 Z. P. Yu, Z. X. Liu, F. X. Chen, R. Qin, T. K. Lau, J. L. Yin, X. Kong, X. Lu, M. Shi, C. Z. Li and H. Chen, *Nat. Commun.*, 2019, **10**, 2152.
19 S. Feng, M. Li, N. Tang, X. Wang, H. Huang, G. Ran, Y. Liu, Z. Xie, W. Zhang and Z. Bo, *ACS Appl. Mater. Interfaces*, 2020, **12**, 4638–4648.
20 H. Lai, H. Chen, Y. Zhu, L. Chen, H.-H. Huang and F. He, *J. Mater. Chem. A*, 2020, **8**, 9670–9676.

21 J. Lee, S. Song, J. Huang, Z. Du, H. Lee, Z. Zhu, S.-J. Ko, T.-Q. Nguyen, J. Y. Kim, K. Cho and G. C. Bazan, *ACS Mater. Lett.*, 2020, **2**, 395–402.
22 J. Lee, S.-J. Ko, H. Lee, J. Huang, Z. Zhu, M. Seifrid, J. Vollbrecht, V. V. Brus, A. Karki, H. Wang, K. Cho, T.-Q. Nguyen and G. C. Bazan, *ACS Energy Lett.*, 2019, **4**, 1401–1409.
23 B. Jia, J. Wang, Y. Wu, M. Zhang, Y. Jiang, Z. Tang, T. P. Russell and X. Zhan, *J. Am. Chem. Soc.*, 2019, **141**, 19023–19031.
24 J. Zhang, W. Liu, S. Chen, S. Xu, C. Yang and X. Zhu, *J. Mater. Chem. A*, 2018, **6**, 22519–22525.
25 C. Li, Y. Xie, B. Fan, G. Han, Y. Yi and Y. Sun, *J. Mater. Chem. C*, 2018, **6**, 4873–4877.
26 C. Li, J. Song, Y. Cai, G. Han, W. Zheng, Y. Yi, H. S. Ryu, H. Y. Woo and Y. Sun, *J. Energy Chem.*, 2020, **40**, 144–150.
27 J. Cao, S. Qu, L. Yang, H. Wang, F. Du, J. Yu and W. Tang, *Chem. Eng. J.*, 2021, **412**, 128770.
28 W. Gao, X. Ma, Q. An, J. Gao, C. Zhong, F. Zhang and C. Yang, *J. Mater. Chem. A*, 2020, **8**, 14583–14591.
29 X. Wang, Z. Du, K. Dou, H. Jiang, C. Gao, L. Han and R. Yang, *Adv. Energy Mater.*, 2019, **9**, 1802530.
30 J. Hou, H. Chen, S. Zhang, G. Li and Y. Yang, *J. Am. Chem. Soc.*, 2008, **130**, 16144.
31 E. Wang, L. Wang, L. Lan, C. Luo, W. Zhuang, J. Peng and Y. Cao, *Appl. Phys. Lett.*, 2008, **92**, 03307.
32 R. C. Coffin, J. Peet, J. Rogers and G. C. Bazan, *Nat. Chem.*, 2009, **1**, 657.
33 R. S. Ashraf, Z. Chen, D. S. Leem, H. Bronstein, W. Zhang, B. Schroed-er, Y. Geerts, J. Smith, S. Watkins, T. D. Anthopoulos, H. Sirringhaus, J. C. de Mello, M. Heeney and I. McCulloch, *Chem. Mater.*, 2011, **23**, 768.
34 Y. Nian, Z. Wang, H. Jiang, S. Feng, S. Li, L. Zhang, Y. Cao and J. Chen, *Chin. J. Chem.*, 2018, **36**, 495–501.
35 Y.-Q.-Q. Yi, H. Feng, N. Zheng, X. Ke, B. Kan, M. Chang, Z. Xie, X. Wan, C. Li and Y. Chen, *Chem. Mater.*, 2019, **31**, 904–911.
36 Y. Sun, G. C. Welch, W. L. Leong, C. J. Takacs, G. C. Bazan and A. J. Heeger, *Nat. Mater.*, 2012, **11**, 44–48.
37 S. Dai, F. Zhao, Q. Zhang, T. K. Lau, T. Li, K. Liu, Q. Ling, C. Wang, X. Lu, W. You and X. Zhan, *J. Am. Chem. Soc.*, 2017, **139**, 1336–1343.
38 Y. Cui, H. Yao, J. Zhang, T. Zhang, Y. Wang, L. Hong, K. Xian, B. Xu, S. Zhang, J. Peng, Z. Wei, F. Gao and J. Hou, *Nat. Commun.*, 2019, **10**, 2515.
39 X. Zhang, L. Qin, J. Yu, Y. Li, Y. Wei, X. Liu, X. Lu, F. Gao and H. Huang, *Angew. Chem., Int. Ed.*, 2021, **133**, 12583–12589.
40 H. Yao, L. Ye, J. Hou, B. Jang, G. Han, Y. Cui, G. M. Su, C. Wang, B. Gao, R. Yu, H. Zhang, Y. Yi, H. Y. Woo, H. Ade and J. Hou, *Adv. Mater.*, 2017, 29.
41 H. Zhang, H. Yao, J. Hou, J. Zhu, J. Zhang, W. Li, R. Yu, B. Gao, S. Zhang and J. Hou, *Adv. Mater.*, 2018, **30**, e1800613.
42 J.-w Ock, D. Kim, H. Kim, H. Jung, H. J. Son, M. J. Ko, J. Koh and B. Kim, *Dyes Pigm.*, 2017, **137**, 445–455.
43 H. Huang, Q. Guo, S. Feng, C. Zhang, Z. Bi, W. Xue, J. Yang, J. Song, C. Li, X. Xu, Z. Tang, W. Ma and Z. Bo, *Nat. Commun.*, 2019, **10**, 3038.
44 G.-Z. Yuan, H. Fan, S.-S. Wan, Z. Jiang, Y.-Q. Liu, K.-K. Liu, H.-R. Bai, X. Zhu and J.-L. Wang, *J. Mater. Chem. A*, 2019, **7**, 20274–20284.
45 J. Wang, W. Wang, X. Wang, Y. Wu, Q. Zhang, C. Yan, W. Ma, W. You and X. Zhan, *Adv. Mater.*, 2017, **29**, 1702125.
46 P. W.-M. Blom, V. D. Mihailetchi, L. J.-A. Koster and D. E. Markov, *Adv. Mater.*, 2007, **19**, 1551–1566.
47 S. Liu, J. Yuan, W. Deng, M. Luo, Y. Xie, Q. Liang, Y. Zou, Z. He, H. Wu and Y. Cao, *Nat. Photonics*, 2012, **14**, 300.
48 Y. Xie, T. Li, J. Guo, P. Bi, X. Xue, H. S. Ryu, Y. Cai, J. Min, L. Huo, X. Hao, H. Y. Woo, X. Zhan and Y. Sun, *Energy Lett.*, 2019, **4**, 1196–1203.
49 T. Wang, R. Sun and W. Wang, *et al.*, *Chem. Mater.*, 2021, **33**, 761–773.
50 X. Xu, L. Yu, H. Yan, R. Li and Q. Peng, *Energy Environ. Sci.*, 2020, **13**, 4381–4388.
51 L. Yang, S. Zhang, C. He, J. Zhang, Y. Yang, J. Zhu, Y. Cui, W. Zhao, H. Zhang, Y. Zhang, Z. Wei and J. Hou, *Chem. Mater.*, 2018, **30**, 2129–2134.
52 H. Hu, Y. Li, J. Zhang, Z. Peng, L.-k Ma, J. Xin, J. Huang, T. Ma, K. Jiang, G. Zhang, W. Ma, H. Ade and H. Yan, *Adv. Energy Mater.*, 2018, **8**, 1800234.
53 S. Pang, R. Zhang, C. Duan, S. Zhang, X. Gu, X. Liu, F. Huang and Y. Cao, *Adv. Energy Mater.*, 2019, **9**, 1901740.
54 H. Wu, H. Fan, S. Xu, L. Ye, Y. Guo, Y. Yi, H. Ade and X. Zhu, *Small*, 2019, **15**, e1804271.
55 Y. Zhang, C.-e Zhang, H. Huang, H. Jin, Y. Gao, R. Zheng, J. Song, C. Li, Z. Ma and Z. Bo, *Dyes Pigm.*, 2021, **184**, 108789.
56 Z. Zhang and X. Zhu, *J. Mater. Chem. A*, 2018, **6**, 4266–4270.